Evolution of the early Antarctic ice ages

Diederik Liebrand[a,1], Anouk T. M. de Bakker[b,c], Helen M. Beddow[d], Paul A. Wilson[a], Steven M. Bohaty[a], Gerben Ruessink[b], Heiko Pälike[e], Sietske J. Batenburg[f,g], Frederik J. Hilgen[d], David A. Hodell[h], Claire E. Huck[a], Dick Kroon[i], Isabella Raffi[j], Mischa J. M. Saes[d], Arnold E. van Dijk[d], Lucas J. Lourens[d]

[a]National Oceanography Centre Southampton, University of Southampton, Southampton, UK

[b]Department of Physical Geography, Faculty of Geosciences, Utrecht University, Utrecht, The Netherlands

[c]Littoral Environnement et Sociétés (LIENSs), Université de La Rochelle, La Rochelle, France

[d]Department of Earth Sciences, Faculty of Geosciences, Utrecht University, Utrecht, The Netherlands

[e]MARUM–Center for Marine Environmental Sciences, University of Bremen, Bremen, Germany

[f] Institute of Geosciences, Goethe-University Frankfurt am Main, Frankfurt, Germany

[g]Department of Earth Sciences, University of Oxford, Oxford, UK

[h]Department of Earth Sciences, University of Cambridge, Cambridge, UK

[i]School of GeoSciences, Grant Institute, University of Edinburgh, Edinburgh, UK

[j]Dipartimento di Ingegneria e Geologia (InGeo), Università degli Studi “G. d’Annunzio” di Chieti–Pescara, Chieti Scalo, Italy

Abstract

Understanding the stability of the early Antarctic ice cap in the geological past is of societal interest because present-day atmospheric CO_2 concentrations have reached values comparable to those estimated for the Oligocene and the early Miocene epochs. Here we analyze a new high-resolution deep-sea oxygen isotope ($\delta^{18}O$) record from the South Atlantic Ocean spanning an interval between 30.1 and 17.1 Myr ago. The record displays major oscillations in deep-sea temperature and Antarctic ice volume in response to the ~110-kyr eccentricity-modulation of precession. Conservative minimum ice volume estimates show that waxing and waning of at least ~85 to 110% the volume of the present East Antarctic Ice Sheet is required to explain many of the ~110-kyr cycles. Antarctic ice sheets were typically largest during repeated glacial cycles of the 'mid' Oligocene (~28.0 to ~26.3 Myr ago) and across the Oligocene-Miocene Transition (~23.0 Myr ago). Yet, the high-amplitude glacial-interglacial cycles of the mid Oligocene are highly symmetrical, indicating a more direct response to eccentricity-modulation of precession than their early Miocene counterparts, which are distinctly asymmetrical – indicative of prolonged ice build up and delayed, but rapid, glacial terminations. We hypothesize that the long-term transition to a warmer climate state with sawtoothed shaped glacial cycles in the early Miocene was brought about by subsidence and glacial erosion in West Antarctica during the late Oligocene and/or a change in the variability of atmospheric CO_2 levels on astronomical time scales that is not yet captured in existing proxy reconstructions.

Keywords

unipolar icehouse, early Antarctic ice sheet, Oligocene-Miocene, glacial-interglacial cycle geometries, bispectral analysis

Significance

The Antarctic ice cap waxed and waned on astronomical time scales throughout the Oligo-Miocene time interval. We quantify geometries of Antarctic ice age cycles, as expressed in a new climate record from the South Atlantic Ocean, to track changing dynamics of the unipolar icehouse climate state. We document numerous ~110-thousand year long oscillations between a near-fully glaciated and deglaciated Antarctica that transitioned from being symmetric in the Oligocene to asymmetric in the Miocene. We infer that distinctly asymmetric ice age cycles are not unique to the late Pleistocene or to extremely large continental ice sheets. The patterns of long-term change in Antarctic climate interpreted from this record are not readily reconciled with existing CO_2 records.

Author contributions: D.L., H.M.B., M.J.M.S., and A.E.D. generated the data. D.L. and A.T.M.B. performed the statistical analyses. D.L., A.T.M.B., P.A.W., and S.M.B. wrote the manuscript. All authors designed the study, discussed the results and commented on the manuscript.

[1] To whom correspondence should be addressed. Email: diederik.liebrand@noc.soton.ac.uk

\body

Introduction

The early icehouse world of the Oligocene and early Miocene epochs (hereafter referred to as Oligo-Miocene) is bracketed by two major climate events: the Eocene-Oligocene Climate Transition (~34 Myr ago, EOT) and the onset of the Middle Miocene Climatic Optimum (~17 Myr ago) (1). Deep-sea proxy records and sedimentological evidence from the Antarctic continental shelves indicate the expansion of continental-size ice sheets on Antarctica at the EOT (2, 3), and sedimentary records from the western Ross Sea on the East Antarctic margin document large subsequent oscillations in ice-sheet extent on astronomical time scales during the Oligo-Miocene (4). In contrast, large ice sheets did not develop in the high northern latitudes until the late Pliocene (5). Thus, the Oligo-Miocene presents an opportunity to study the dynamics of a unipolar (Antarctic) icehouse climate state without the overprint of Northern Hemisphere ice sheets on benthic foraminiferal $\delta^{18}O$ records. Published proxy records of atmospheric CO_2 concentration show a decline from the Oligocene to the Miocene (6, 7) that is broadly contemporaneous with a strong minimum in the ~2.4 Myr eccentricity cycle at ~24 Myr ago (8), which would promote continental ice sheet expansion if radiative forcing was the dominant control on ice volume. Previous studies using drill-core records from the deep ocean demonstrate a climatic response to astronomical forcing for the Oligocene (9, 10) and parts of the Miocene (11-13). Yet to improve understanding of the behavior of the climate/cryosphere system we need longer high-resolution records from strategic locations that capture the changing response of the high latitudes to the combined effects of CO_2, astronomical forcing and tectonic boundary conditions.

Walvis Ridge Ocean Drilling Program Site 1264

To shed new light on southern high-latitude climate variability through the Oligo-Miocene, we analyze a new high-resolution benthic foraminiferal $\delta^{18}O$ record from Walvis Ridge, located in the southeastern Atlantic Ocean (Ocean Drilling Program Site 1264; 2505 m water depth; 2000–2200 m paleo-water depth; 28.53°S, 2.85°E, Fig. 1; (14, 15)). An astrochronology for Site 1264 was developed by tuning $CaCO_3$ estimates to the stable eccentricity solution independently of the benthic $\delta^{18}O$ record (15). On the eccentricity-tuned age model, the Site 1264 record spans a 13-Myr time window between 30.1 and 17.1 Myr ago and ranges between 405-kyr Eccentricity Cycles 74–43 and ~2.4-Myr Eccentricity Cycles 13–8 (Fig. 1; (15)), representing the first continuous record from a single site spanning the 'mid' Oligocene to early Miocene. Five distinct time intervals with clear multi-Myr climatic trends are identified in this new $\delta^{18}O$ dataset from Walvis Ridge: (i) an early Oligocene time interval of climate deterioration (~30.1–28.0 Myr ago); (ii) a generally cold but highly unstable mid-Oligocene time interval (~28.0–26.3 Myr ago), which we refer to as the Mid Oligocene Glacial Interval (MOGI); (iii) a late Oligocene time interval characterized by low-amplitude climate variability and stepwise climatic amelioration (~26.3–23.7 Myr ago), confirming that this warming trend is a real feature of Cenozoic climate history (9) rather than an artifact of composite records from multiple sites in different ocean basins; (iv) a time interval of persistently high-amplitude climate variability spanning the Oligocene-Miocene Transition (OMT) and the earliest Miocene (~23.7–20.4 Myr ago); and (v) a time interval of moderate-amplitude climate variability during the latter part of the early Miocene (~20.4–17.1 Myr ago).

Following the MOGI, the late Oligocene warming phase proceeded in a series of three distinct steps (~26.3, ~25.5, and ~24.2 Myr ago), with the peak warming/lowest ice volume confined to a ~500 kyr period (~24.2–23.7 Myr ago). This climate state was terminated by the OMT (~23.7–22.7 Myr ago), which consists of two rapid ~0.5‰ increases in benthic δ^{18}O that are separated by an interval (405-kyr eccentricity cycle long) of partial δ^{18}O recovery (15). The onset of the OMT is thereby comparable in structure to the EOT (3). A 405-kyr long overall decrease in benthic δ^{18}O marks the recovery phase of the OMT.

Ice volume estimates

To better understand the significance of the documented δ^{18}O variability on long-term change in the high-latitude climate system, we make a conservative estimate of the minimum contribution of continental ice volume to the Site 1264 benthic δ^{18}O signal by assuming that Oligo-Miocene bottom-water temperatures at Site 1264 were never colder than the current temperature of 2.5°C and applying an average δ^{18}O composition of Oligo-Miocene ice sheets ($\delta^{18}O_{ice}$) of −42‰ VSMOW (see Methods; (16)). These minimum ice volume estimates (Fig. 1) do not fully account for the changing relative contributions of ice volume and deep-sea temperature to the benthic δ^{18}O signal over glacial-interglacial cycles. However, they are largely consistent with estimates of glacioeustatic sea level change from the New Jersey shelf (17) and those generated by inverse models of (multi-site composite) δ^{18}O records (12, 18). These ice volume estimates and sea level reconstructions strongly suggest that a very large part of the benthic $\delta^{18}O$ signal is linked to large ice volume changes on Antarctica.

Three major new results stand out in the minimum ice-volume calculations on the Site 1264 benthic $\delta^{18}O$ record (Fig. 1A). First, excluding the OMT interval, the Oligocene glacials are characterized by larger continental ice-sheet volumes than those of the early Miocene, particularly during the MOGI. Second, across the OMT, Antarctica transitioned from a climate state that was fully deglaciated to one characterized by an ice sheet as large as the present East Antarctic Ice Sheet and back into a fully deglaciated state in less than 1 Myr. Third, many glacial-interglacial cycles in the benthic $\delta^{18}O$ record are associated with a $\delta^{18}O_{sw}$ change of at least ~0.60 to 0.75‰, requiring the waxing and waning of ~21 to 26 × 10^6 km^3 of ice, or ~85 to 110% of present East Antarctic ice volume, on timescales of ≤110 kyr.

Sinusoidal glacial-interglacial cycle properties

The 13 Myr-long Oligo-Miocene benthic $\delta^{18}O$ record from Site 1264 shows distinct cyclicity on astronomical time scales. Wavelet analysis reveals (Figs. 1, S1; (15)) that the amplitude of variability at the ~110-kyr eccentricity periodicity is particularly pronounced (≥1.0‰ across the larger $\delta^{18}O$ cycles). The amplitude of the 40-kyr obliquity periodicity is subdued in comparison to published records from other sites, presumably because of the higher sedimentation rates at those sites (13, 19). Four relatively short (405 kyr-long) intervals with particularly strong ~110-kyr-paced $\delta^{18}O$ variability are also identified in the record (vertical gray bars, Fig. 1), demonstrating a pronounced climate-cryosphere response to eccentricity-modulated precession of Earth's spin-axis (15). These intervals are contemporaneous with 405-kyr eccentricity maxima during ~2.4-Myr eccentricity maxima, specifically 405-kyr Cycles 73, 68, 57 and 49. Thus, while the OMT deserves its status as a major transient Cenozoic event (1, 20) because it is a prominent but transient glacial episode that abruptly terminates late Oligocene warming, the amplitude of ice age cycles observed as the climate system emerges from peak glacial OMT conditions is not unique in the Oligo-Miocene. In fact, this recovery phase of the OMT is one of four Oligo-Miocene intervals characterized by particularly high-amplitude ~110-kyr oscillations between glacial and interglacial Antarctic conditions (Fig. 1A). The record from Site 1264 is the first to unequivocally show that the ~2.4-Myr eccentricity cycle paces recurrent episodes of high-amplitude ~110-kyr variability in benthic δ^{18}O (9, 19) and provides a new global climatic context in which to understand Oligo-Miocene glacial history, carbon cycling (9, 21), mid-latitude terrestrial water balance (22) and mammal turnover rates (23) that show similar pacing. The intervals with particularly strong ~110-kyr cycles are separated by prolonged periods of attenuated ~110-kyr cycle amplitude, indicating that not all ~2.4-Myr and 405-kyr eccentricity maxima trigger similar cryospheric responses (Fig. 1). Specifically, ~2.4-Myr Eccentricity Cycle 11 in the late Oligocene is not characterized by high-amplitude ~110-kyr cycles (Fig. 1). Furthermore, no consistent relationship is found between strong ~110-kyr cycles in benthic δ^{18}O and the ~1.2-Myr amplitude modulation of obliquity (15). This suggests that some other factor or combination of factors is responsible for the changing response of the climate system to astronomical forcing on ~110-kyr time scales over the Oligo-Miocene.

We assess the phase-relationships of the tuned δ^{18}O data with respect to the main frequencies of orbital eccentricity to track the response times of the Oligo-Miocene climate system (Figs. 1, S2, S3). The benthic δ^{18}O record from Site 1264 displays a marked multi-Myr evolution in the phasing of the ~110-kyr cycle relative to eccentricity starting with a ~10 kyr phase lag during the mid Oligocene, followed by an unstable phase relation at ~26 Myr ago and a steady increase in phase that culminates in a 10–15 kyr lag at ~19.0 Myr ago (Fig. S3). The ~95-kyr and ~125-kyr frequencies show largely independent phase evolutions. On the basis of these data alone, we cannot rule out the possibility that part of the observed structure in the long-term phase evolution arises from changes in the proportional contribution of temperature and ice volume to benthic δ^{18}O (24). Yet the observed changes in phase are so large (~ –10 kyr to +15 kyr) that changes in the response time of Antarctic ice sheets are most likely responsible; large continental ice sheets are the slowest-responding physical component of Earth's climate system and the only mechanism capable of inducing phase lags in deep-sea benthic δ^{18}O records of ~10–15 kyr (25). Analysis of phasing suggests that over full glacial-interglacial cycles, the high latitude climate–Antarctic ice sheet system responded more slowly to astronomical pacing during the MOGI (~28.0–26.3 Myr ago) and early Miocene ($\lesssim$23 Myr ago), than during either the early Oligocene (~30.1–28.0 Myr ago) or late Oligocene (~26.3–23.7 Myr ago).

Bispectral analysis

To investigate phase coupling between (astronomical) cycles embedded in the Site 1264 benthic $\delta^{18}O$ record, we apply bispectral techniques (26-28). A bispectrum identifies phase-couplings between three frequencies: f_1, f_2 and their sum frequency $f_1 + f_2 = f_3$. When phase coupled, energy transfers nonlinearly between these frequencies and is redistributed over the spectrum. This results in lower and higher harmonics and in the formation of skewed and/or asymmetric cycle geometries such as those observed in the $\delta^{18}O$ record. We compare bispectra for two selected time intervals with strong ~110-kyr cyclicity (Fig. 2): a mid-Oligocene interval, during ~2.4-Myr Eccentricity Cycle 12 (28.30–26.30 Myr ago), and an OMT-spanning interval, during ~2.4-Myr Eccentricity Cycle 10 (23.54–21.54 Myr ago). A third, early Miocene example is considered in Fig. S5. The bispectra show that during both the mid-Oligocene and the OMT numerous phase-couplings occur with frequencies that include, but are not limited to, astronomical cycles. Most interactions occur between cycles with periodicities close to those of eccentricity (periods of 405, ~125 and ~95 kyr/cycle, equal to frequencies of 2.5, 8.0 and 10.5 cycles/Myr respectively) that exchange energy among one another and also with higher frequencies. The close proximity of both positive and negative interactions around eccentricity frequencies (Figs. 2, S4) suggests that these frequencies redistribute energy by broadening spectral peaks in $\delta^{18}O$. This process may explain the observed ~200-kyr cycle (15). The main difference between the two selected time intervals is that the OMT bispectrum reveals many more nonlinear interactions (Fig. 2), both positive and negative, which indicates that the climate/cryosphere system responded in a more complex and indirect manner to insolation forcing across the OMT than during the MOGI. This observation may point to the activation of heightened positive feedback mechanisms across the OMT related to continental ice-sheet growth and decay (13, 29), possibly involving the carbon cycle (30) or Antarctic sea ice (31).

Non-sinusoidal glacial-interglacial cycle properties

To further understand the nonlinearity in the climate system documented by the bispectra, we assess non-sinusoidal (i.e. non-Gaussian) cycle properties (Figs. 3, S5–S8, see also SI Text). Nonlinearity in climate cycles can be quantified in terms of skewness, asymmetry and kurtosis using standard and higher-order spectral analyses to elucidate the rapidity of climatic transitions (see Methods). The remarkably consistent negative skewness in the $\delta^{18}O$ record (mean −0.18, Figs. 3, S8) indicates that Oligo-Miocene glacials were longer in duration than interglacials – a result that is consistent with the late Pleistocene record (Fig. S6; (27, 28, 32)). To assess the time spent per cycle in full glacial and full interglacial conditions (in contrast to skewness which records the duration of glacials versus interglacials), we also calculate the evolution of cycle kurtosis through the benthic $\delta^{18}O$ record. Square-waved (platykurtic) glacial-interglacial cycles are more evident in the Site 1264 record than thin-peaked (leptokurtic) ones, apart from an early Miocene interval between ~21.5 and 19.0 Myr ago when leptokurtic cycles prevail (Figs. 3, S8). This observation indicates that the Oligo-Miocene climate system generally favored full glacial and full interglacial conditions and transitioned rapidly between those two climate states. We attribute this finding to the operation of well-documented strong positive feedbacks on ice sheet growth and decay (25, 29).

To understand the relative rates of ice sheet growth versus decay we quantify cycle asymmetry. While the Site 1264 record shows consistently skewed Oligo-Miocene ~110-kyr glacial-interglacial cycles, we document a major change over time in the symmetry of those cycles that is marked by a transition to more asymmetric cycles which began ~23 Myr ago at the OMT. This change represents a shift to a new climatic state characterized by strong ~2.4-Myr pacing of glacial-interglacial asymmetry and is associated with lower atmospheric CO_2 levels (Fig. 3; (6, 7)) Asymmetry in the data series is particularly pronounced during 405-kyr Eccentricity Cycles 57 and 49 (at ~22.7 and 19.5 Myr ago), which are characterized by distinctly sawtooth-shaped ~110-kyr cycles, suggesting a causal link between cycle amplitude and asymmetry during the early Miocene, but not during the MOGI. The distinctly asymmetric cycles suggest that the early Miocene Antarctic ice sheets periodically underwent intervals of growth that were prolonged relative to astronomical forcing and then underwent subsequent rapid retreat in a manner akin to the glacial terminations of the late Pleistocene glaciations, in which the large ice sheets of the Northern Hemisphere were major participants (27, 28, 32). The highly asymmetric (sawtooth) nature of late Pleistocene glacial-interglacial cycles is thought to originate from a positive ice mass-balance that persists through several precession- and obliquity-paced summer insolation maxima. This results in decreased ice-sheet stability and rapid terminations every ~110 kyr, once the ablation of the Northern Hemisphere ice sheets increases dramatically in response to the next insolation maximum. The increase in ablation is caused by lowered surface elevation of the ice sheets resulting from crustal sinking and delayed isostatic rebound (33). Similar mechanisms are implied for the large Antarctic ice sheets of the OMT (~22.5 Myr ago) but it is less clear why the smaller ice sheets of the early Miocene (~19.5 Myr ago) would exhibit this distinctly sawtoothed pattern of growth and decay (Fig. 3).

Climate–cryosphere evolution

Analysis of the new $\delta^{18}O$ record from Site 1264 raises two important questions: (i) Why did Antarctic ice sheets decrease in size after the OMT? (ii) Why was hysteresis (i.e., glacial-interglacial asymmetry) apparently stronger for both the large OMT and the smaller early Miocene ice sheets than for the large ice sheets of the Oligocene? One explanation for the long-term change in ice volume is that the large glacial ice volumes of the MOGI were possible because of higher topography in West Antarctica (34) that permitted formation of a large terrestrial ice sheet that also buttressed growth of ice sheets on East Antarctica (25, 35). In this interpretation, tectonic subsidence and glacial erosion during the late Oligocene caused a shift to a smaller marine-based ice sheet in West Antarctica (25, 35), which limited the maximum size of the early Miocene Antarctic ice sheets during peak glacial intervals.

The early Miocene ice sheets may have been less responsive to astronomically paced changes in radiative forcing because of colder polar temperatures under lower CO_2 conditions from ~24 Myr ago onwards (7) or restriction of ice sheets to regions of East Antarctica above sea level following the late Oligocene subsidence of West Antarctica (25, 35). Another possibility is that the large ice sheets that characterized the peak glacials of the MOGI underwent rapid major growth and decay because of higher-amplitude glacial-interglacial CO_2 changes than during the early Miocene. Such hypothesized high amplitude changes in CO_2 would have had a direct effect on radiative forcing, which in turn would have caused faster feedbacks and a more linear response to eccentricity-modulation of precession. Given that larger ice volumes are to be expected in a climatic state that is characterized by high cycle asymmetry and low atmospheric CO_2 concentration, a third possibility is that the conservative calculations substantially underestimate true ice volumes for the early Miocene. Each of these hypotheses can be tested through a combination of scientific drilling on the West Antarctic shelf margin and development of high-resolution CO_2 and marine temperature proxy records with astronomical age control. We predict that strong eccentricity-driven CO_2 cycles (~110, 405, & ~2400 kyr) that are closely in-step with ice volume changes will emerge in proxy CO_2 reconstructions for the Oligo-Miocene time interval. Assuming that changes in partitioning of the benthic $\delta^{18}O$ signal between temperature and ice volume are modest throughout the Oligo-Miocene, the deep-sea $\delta^{18}O$ record from Site 1264 suggests a clear long-term shift from a more glacial Oligocene to a less glacial early Miocene climate state – a pattern of change not readily reconciled with the long-term decrease in published CO_2 records.

Acknowledgments: We thank David Heslop and Lie-Liang Yang for insightful discussions and assistance. We used samples provided by the Ocean Drilling Program, sponsored by the US National Science Foundation and participating countries under the management of the Joint Oceanographic Institutions. We are greatly indebted to the scientists and supporting staff of ODP Leg 208. This research was made possible by funding of ERC grants 215458 ("GTS-NEXT", F.J.H.) and 617462

("EARTHSEQUENCING", H.P.), NWO grants 864.02.007 (L.J.L.), 865.10.001 (L.J.L.), and 821.01.012 (G.R.), NERC grant NE/K014137/1 (P.A.W.), and a Royal Society Wolfson award (P.A.W.).

References

1. Zachos JC, Dickens GR, & Zeebe RE (2008) An early Cenozoic perspective on greenhouse warming and carbon-cycle dynamics. *Nature* 451(7176):279-283.
2. Zachos JC, Breza JR, & Wise SW (1992) Early Oligocene ice-sheet expansion on Antarctica: Stable isotope and sedimentological evidence from Kerguelen Plateau, southern Indian Ocean. *Geology* 20:569 - 573.
3. Coxall HK, Wilson PA, Pälike H, Lear CH, & Backman J (2005) Rapid stepwise onset of Antarctic glaciation and deeper calcite compensation in the Pacific Ocean. *Nature* 433(7021):53-57.
4. Naish TR*, et al.* (2001) Orbitally induced oscillations in the East Antarctic ice sheet at the Oligocene/Miocene boundary. *Nature* 413:719-723.
5. Bailey I*, et al.* (2013) An alternative suggestion for the Pliocene onset of major northern hemisphere glaciation based on the geochemical provenance of North Atlantic Ocean ice-rafted debris. *Quaternary Science Reviews* 75:181 - 194.
6. Beerling DJ & Royer DL (2011) Convergent Cenozoic CO_2 history. *Nature Geoscience* 4:418 - 420.
7. Zhang YG, Pagani M, Liu Z, Bohaty S, & DeConto R (2013) A 40-million-year history of atmospheric CO_2. *Phil. Trans. R. Soc. A* 371.

8. Laskar J, Gastineau M, Delisle J-B, Farrés A, & Fienga A (2011) Strong chaos induced by close encounters with Ceres and Vesta. *Astronomy and Astrophysics* 532(L4):1-4.
9. Pälike H*, et al.* (2006) The heartbeat of the Oligocene climate system. *Science* 314:1894-1898.
10. Wade BS & Pälike H (2004) Oligocene climate dynamics. *Paleoceanography* 19(4).
11. Holbourn A, Kuhnt W, Kochhann KGD, Andersen N, & Meier KJS (2015) Global perturbation of the carbon cycle at the onset of the Miocene Climatic Optimum. *Geology*.
12. Liebrand D*, et al.* (2011) Antarctic ice sheet and oceanographic response to eccentricity forcing during the early Miocene. *Climate of the Past* 7:869-880.
13. Zachos JC, Shackleton NJ, Revenaugh JS, Palike H, & Flower BP (2001) Climate response to orbital forcing across the Oligocene-Miocene boundary. *Science* 292(5515):274-278.
14. Zachos JC*, et al.* (2004) Initial Reports: Leg 208. in *Proceedings of the Ocean Drilling Program* (Ocean Drilling Program).
15. Liebrand D*, et al.* (2016) Cyclostratigraphy and eccentricity tuning of the early Oligocene through early Miocene (30.1–17.1 Ma): *Cibicides mundulus* stable oxygen and carbon isotope records from Walvis Ridge Site 1264. *Earth and Planetary Science Letters* 450:392-405.
16. DeConto RM*, et al.* (2008) Thresholds for Cenozoic bipolar glaciation. *Nature* 455:652-656.

17. Miller KG*, et al.* (2005) The phanerozoic record of global sea-level change. *Science* 310(5752):1293-1298.

18. De Boer B, Van de Wal RSW, Bintanja R, Lourens LJ, & Tuenter E (2010) Cenozoic global ice-volume and temperature simulations with 1-D ice-sheet models forced by benthic δ^{18}O records. *Annals of Glaciology* 51(55):23-33.

19. Pälike H, Frazier J, & Zachos JC (2006) Extended orbitally forced palaeoclimatic records from the equatorial Atlantic Ceara Rise. *Quaternary Science Reviews* 25(23-24):3138-3149.

20. Beddow HM, Liebrand D, Sluijs A, Wade BS, & Lourens LJ (2016) Global change across the Oligocene-Miocene Transition: High-resolution stable isotope records from IODP Site U1334 (equatorial Pacific Ocean). *Paleoceanography* 31:81–97

21. Valero L, Cabrera L, Sáez A, & Garcés M (2016) Long-period astronomically-forced terrestrial carbon sinks. *Earth and Planetary Science Letters* 444:131–138.

22. Valero L, Garcés M, Cabrera L, Costa E, & Sáez A (2014) 20 Myr of eccentricity paced lacustrine cycles in the Cenozoic Ebro Basin. *Earth and Planetary Science Letters* 408:183 - 193.

23. Van Dam JA*, et al.* (2006) Long-period astronomical forcing of mammal turnover. *Nature* 443(7112):687-691.

24. Elderfield H*, et al.* (2012) Evolution of ocean temperature and ice volume through the mid-Pleistocene climate transition. *Science* 337:704 - 709.

25. Gasson E, DeConto RM, Pollard D, & Levy RH (2016) Dynamic Antarctic ice sheet during the early to mid-Miocene. *P Natl Acad Sci USA* 113(13):3459-3464.

26. Hasselmann K, Munk W, & MacDonald G (1963) Bispectra of ocean waves. *Proceedings of the Symposium on Time Series Analysis*, ed Rosenblatt M (John Wiley), pp 125-139.

27. Hagelberg T, Pisias N, & Elgar S (1991) Linear and nonlinear couplings between orbital forcing and the marine $\delta^{18}O$ record during the late Neogene. *Paleoceanography* 6(6):729 - 746.

28. King T (1996) Quantifying nonlinearity and geometry in time series of climate. *Quaternary Science Reviews* 15:247 - 266.

29. DeConto RM & Pollard D (2016) Contribution of Antarctica to past and future sea-level rise. *Nature* 531(7596):591-597.

30. Mawbey EM & Lear CH (2013) Carbon cycle feedbacks during the Oligocene-Miocene transient glaciation. *Geology* 41(9):963-966.

31. DeConto R, Pollard D, & Harwood D (2007) Sea ice feedback and Cenozoic evolution of Antarctic climate and ice sheets. *Paleoceanography* 22(3).

32. Lisiecki LE & Raymo ME (2007) Plio-Pleistocene climate evolution: trends and transitions in glacial cycle dynamics. *Quaternary Science Reviews* 26(1-2):56-69.

33. Abe-Ouchi A*, et al.* (2013) Insolation-driven 100,000-year glacial cycles and hysteresis of ice-sheet volume. *Nature* 500:190-194.

34. Fretwell P*, et al.* (2013) Bedmap2: improved ice bed, surface and thickness datasets for Antarctica. *Cryosphere* 7(1):375-393.

35. Levy R*, et al.* (2016) Antarctic ice sheet sensitivity to atmospheric CO_2 variations in the early to mid-Miocene. *P Natl Acad Sci USA* 113(13):3453-3458.

36. Miller KG, Fairbanks RG, & Mountain GS (1987) Tertiary Oxygen Isotope Synthesis, Sea Level History, and Continental Margin Erosion. *Paleoceanography* 2(1):1-19.

37. Marchitto TM*, et al.* (2014) Improved oxygen isotope temperature calibrations for cosmopolitan benthic foraminfera. *Geochimica et Cosmochimica Acta* 130:1 - 11.

38. Schlitzer R (2010) Ocean Data View 4, version 4.3.6, http://odv.awi.de).

39. Bohaty SM, Zachos JC, & Delaney ML (2012) Foraminiferal Mg/Ca evidence for Southern Ocean cooling across the Eocene–Oligocene transition. *Earth and Planetary Science Letters* 317-318:251–261.

40. Petersen SV & Schrag DP (2015) Antarctic ice growth before and after the Eocene-Oligocene transition: New estimates from clumped isotope paleothermometry. *Paleoceanography* 30:1305-1317.

41. Bamber JL, Layberry RL, & Gogineni S (2001) A new ice thickness and bed data set for the Greenland ice sheet 1. Measurement, data reduction, and errors. *J Geophys Res-Atmos* 106(D24):33773-33780.

42. Charette MA & Smith WHF (2010) The Volume of Earth's Ocean. *Oceanography* 23(2):112-114.

43. Paillard D, Labeyrie L, & Yiou P (1996) AnalySeries, Macintosh program performs time-series analysis. *EOS Transactions AGU* 77(39):379.

44. Beddow HM*, et al.* (2016) Early to middle Miocene climate evolution: benthic oxygen and carbon isotope records from Walvis Ridge Site 1264. *Orbital forcing and climate response; astronomicallly-tuned age models and stable isotope*

records for the Oligocene-Miocene, ed Beddow HM (Utrecht University, Utrecht), Vol PhD.

45. Chaudhuri P & Marron JS (1999) SiZer for exploration of structures in curves. *Journal of the American Statistical Association* 94(447):807 - 823.

46. Herbers THC, Russnogle NR, & Elgar S (2000) Spectral energy balance of breaking waves within the surf zone. *Journal of Physical Oceanography* 30:2723 - 2737.

47. Elgar S (1987) Relationships involving third moments and bispectra of a harmonic process. *IEEE Transactions of Acoustics, Speech, and Signal Processing* ASSP-35(12):1725 - 1726.

48. De Bakker ATM, Herbers THC, Smit PB, Tissier MFS, & Ruessink BG (2015) Nonlinear infragravity-wave interactions on a gently sloping laboratory beach. *Journal of Physical Oceanography* 45:589 - 605.

49. Doering JC & Bowen AJ (1995) Parametrization of orbital velocity asymmetries of shoaling and breaking waves using bispectral analysis. *Coastal Engineering* 26:15-33.

50. Kennedy AB, Chen Q, Kirby JT, & Dalrymple RA (2000) Boussinesq modeling of wave transformation, breaking, and runup. I:1d. *Journal of waterway, port, coastal, and ocean engineering*:39-47.

51. Pearson K (1905) Skew variation, a rejoinder. *Biometrika* IV:169-212.

52. Herbert TD (1994) Reading orbital signals distorted by sedimentation: models and examples. *Spec. Publs Int. Ass. Sediment* 19:483-507.

53. Bard E (2001) Paleoceanographic implications of the difference in deep-sea sediment mixing between large and fine particles. *Paleoceanography* 16(2):235 - 239.

54. Lisiecki LE & Raymo ME (2005) A Pliocene-Pleistocene stack of 57 globally distributed benthic δ^{18}O records. *Paleoceanography* 20.

Figure Legends

Fig. 1. High-latitude climate/cryosphere evolution during the Oligo-Miocene and sinusoidal glacial-interglacial cycle properties. (A) Benthic foraminiferal (*Cibicides mundulus*) δ^{18}O record from ODP Site 1264 (gray line; (15)) and SiZer smooth (blue line, see Methods). Minimum ice volume contribution (lilac area, right axis) to the benthic δ^{18}O record calculated relative to all values exceeding 1.65‰ (left axis, see Methods). Dashed red line represents the contribution to benthic δ^{18}O of a present day-sized East Antarctic Ice Sheet ($\delta^{18}O_{ice} = -42$‰). (B–D) Sinusoidal glacial-interglacial cycle properties. (B) Wavelet analysis of the Site 1264 benthic δ^{18}O record. White dashed lines represent the ~95- and ~125-kyr eccentricity periodicities, respectively. (C) Filter of the Site 1264 benthic δ^{18}O record centered around the ~110-kyr periodicity (dark blue line) and its amplitude modulation (light blue line and area), compared to those of eccentricity (gray lines and area). The filter values are proportional to the eccentricity (left axis) and the VPDB scale (right axis), respectively. In the background (light brown line and area) the ~2.4-Myr component of Earth's orbital eccentricity is shown (+0.02, brown bold italic numbers). (D) Phase-evolution of the ~125-kyr (dark blue area, green dots) ~95-kyr (purple area, brown dots) and combined (including intermediate frequencies) ~110-kyr

(light blue area, orange dots) cycle to eccentricity, which show independent evolutions. Vertical gray bars represent 405-kyr Eccentricity Cycles 49, 57, 68 and 73 (dark gray italic numbers), characterized by exceptionally strong ~110-kyr responses in benthic δ^{18}O (Fig. 3; (15)).

Fig. 2. Bispectra assessing phase coupling and energy transfers between frequencies in the δ^{18}O data. Bispectral analyses on benthic δ^{18}O across two, 2-Myr long windows with strong ~110-kyr cycles (see also Fig. S4). (A) Bispectrum across the OMT interval, during ~2.4-Myr Eccentricity Cycle 10 (23.54–21.54 Myr ago). (B) Bispectrum across the MOGI, during ~2.4-Myr Eccentricity Cycle 12 (28.30–26.30 Myr ago). The colors of the bispectrum show the direction of the energy transfers. The intensity of the colors is indicative of the magnitude of energy transfers (see Methods). Red indicates a transfer of spectral power from two frequencies f_1 (see x-axes) and f_2 (see y-axes), to frequency f_3 ($f_1 + f_2 = f_3$). In contrast, blue represents a gain of spectral power at frequencies f_1 and f_2, from frequency f_3. Gray lines reflect the main astronomical frequencies of eccentricity, obliquity and precession.

Fig. 3. Non-sinusoidal glacial-interglacial cycle properties. (A) Atmospheric CO_2 proxy estimates for the Oligo-Miocene and their long-term smooths (turquoise line and area, see Methods) through the reconstructed values and their maximum and minimum error estimates (black error bars). Gray diamonds represent phytoplankton CO_2 estimates, yellow squares are based on stomata, and purple-red triangles represent CO_2 estimates based on paleosols (6, 7). Multiplication factors on the right refer to pre-industrial (p.-i.)

CO_2 concentrations of 278 ppm. CE stands for Common Era. (B-E) Four 405-kyr long intervals with exceptionally strong ~110-kyr cycles in benthic $\delta^{18}O$, plotted against eccentricity and its ~2.4-Myr component (+0.02). These intervals occur during (B) the early Miocene, contemporaneous with 405-kyr Eccentricity Cycle 49, (C) the Oligo-Miocene transition, Cycle 57, (D) the mid-Oligocene, Cycle 68, and (E) the early Oligocene, Cycle 73 (white italic numbers). For panels (B-E) only: long ticks on the age-axis indicate 500 kyr steps and short ticks 100 kyr steps. (F–H) Non-sinusoidal glacial-interglacial cycle properties. (F) Skewness, (G) Asymmetry, and (H) Kurtosis of the Site 1264 benthic $\delta^{18}O$ record quantified over a 2-Myr long sliding window using standard (turquoise circles) and bispectral (purple-pink triangles) methods (see Methods). The colored areas indicate the 2σ upper and lower ranges of asymmetry. (I) Earth's orbital eccentricity (8) and its ~2.4-Myr component (+0.02, brown bold italic). Vertical gray bars as in Fig. 1. To the right of panels F-H the corresponding cycle shapes are depicted and the direction of time is indicated; ig = interglacial, g = glacial.

Supporting Information

Materials and Methods:

All data reported in this paper are available online. Go to: www.pangaea.de, and search for ref. (15), or follow the link: https://doi.pangaea.de/10.1594/PANGAEA.862589.

Ice volume calculations. To obtain conservative minimum estimates of continental ice volume (36) across the Oligo-Miocene study interval, we calculated a *Cibicides* δ^{18}O ($\delta^{18}O_{Cib}$) value from equation 9 of (37) using (i) the modern Site 1264 bottom-water temperatures of ~2.5 °C (38) and (ii) an 'ice-free' seawater δ^{18}O ($\delta^{18}O_{sw}$) value of −1.05‰ VSMOW (39, 40). This gives a $\delta^{18}O_{Cib}$ value of 1.65‰ VPDB, indicating that values ≥1.65‰ reflect a change in $\delta^{18}O_{sw}$ and, hence, a contribution from land ice to the $\delta^{18}O_{Cib}$ signal, presuming that Oligo-Miocene deep-water temperatures at Site 1264 never cooled below modern-day temperatures. To estimate the minimum Oligo-Miocene land ice volumes, we applied an ice-free ocean volume of $\sim 1.3574 \times 10^9$ km^3 (34, 41, 42) and used a modeled average δ^{18}O value of Oligo-Miocene ice sheets of −42‰ VSMOW (16), which yields ~3.8 million km^3 of ice per 0.1‰ change in seawater δ^{18}O. This approach does not account for decreasing $\delta^{18}O_{ice}$ through the glacial cycle as the ice sheet becomes larger and higher in elevation. But state-of-the-art ice sheet models show that once a large Antarctic ice sheet is established, the average $\delta^{18}O_{ice}$ must have been quite low (−39 to −48‰; (25)). If we assume that $\delta^{18}O_{ice}$ was higher than −40‰, calculated ice volumes are unrealistically large. These ice volume estimates are calculated to show that the ice-volume component of the benthic δ^{18}O record must have been large and that the sinusoidal and non-sinusoidal cycle properties that we quantify are most likely related to Antarctic ice sheet dynamics. We note that the cycle properties, or their long-term evolution, may partially reflect changing relative contributions of temperature and ice volume to benthic $\delta^{18}O$. Both the Gaussian and the non-Gaussian statistics are applied to the benthic $\delta^{18}O$ record and are thus independent from the exact amount of ice volume contribution to benthic $\delta^{18}O$.

Sinusoidal cycle properties. All data were resampled at 2.5 kyr and for $CaCO_3$ est. and $\delta^{18}O$ periodicities >1 Myr were removed using a notch filter (frequency = 0.0 cycles/Myr, bandwidth = 1.0 cycle/Myr) prior to statistical analyses (43). To calculate phases and non-sinusoidal cycle shapes between 18.1 and 17.1 Myr ago, the $CaCO_3$ est. and $\delta^{18}O$ data from (44) between 17.1 and 16.1 Myr ago were used, as 2-Myr windows were required to perform these statistical analyses. The time-frequency transforms of $\delta^{18}O$ were computed using an adaptation of a wavelet script (Figs. S1, S2; (15)), and for the wavelet analysis only, periodicities greater than 200 kyr were removed from the $\delta^{18}O$ record using a notch filter (43). Gaussian filtering of the ~110-kyr component of the $\delta^{18}O$ record and a Hilbert transform of the filtered data were calculated to compute the ~110-kyr amplitude modulation (frequencies between 6.4 and 12.4 cycles/Myr for Fig. 1b; frequency = 9.4 cycles/Myr, bandwidth = 3.0 cycles/Myr for Fig. S1b). Phase calculations of $CaCO_3$ est. and $\delta^{18}O$ relative to eccentricity were calculated across 2-Myr windows with 250-kyr time steps through Blackman-Tukey cross-spectral analysis (43) (Figs. S2, S3). Linear trends were removed, the data were pre-whitened, normalized, and 95% confidence levels on the error bars were computed. This resulted in a frequency resolution of 0.1 cycles/Myr. The frequency bandwidths of 2.2–2.7, 7.4–10.8, 7.4–8.3, and 9.8–10.8 cycles/Myr were used to compute phases for the 405-kyr, ~110-kyr, ~125-kyr and ~95-kyr components, respectively. When coherent, maximum, average and minimum values were selected within these frequency bandwidths to yield phases and their 95% error estimates. Phase estimates are not depicted if none of the frequencies within a bandwidth was coherent. Smooths were taken of the benthic δ^{18}O record, the atmospheric CO_2 data (6, 7) and the non-sinusoidal cycle properties using SiZer (significant zero crossings of derivatives); a statistical method that extracts the structures in curves (Figs. 1, 3, Figs. S6–S8; (45)).

Bispectral analysis. The bispectrum assesses coupling and energy transfers between frequencies within a single time-series. The bispectrum is defined (26) as $B_{f_1, f_2} = E[A_{f_1} A_{f_2} A^*_{f_1+f_2}]$, where $E[]$ is the ensemble average of the triple product of complex Fourier coefficients A at the frequencies f_1, f_2, and their sum $f_1 + f_2$, and the asterisk indicates complex conjugation. The imaginary part of the bispectrum is linked to energy transfers (46) and is therefore shown in Figs. 2 and S4. Oligo-Miocene bispectral settings were: resampling resolution = 2.5 kyr, window length = 2 Myr, step-size = 0.1 Myr, blocks = 8, block length = 1 Myr, degrees of freedom = 16, frequency resolution = 0.001 cycles/kyr (Fig. 2, Figs. S4, S6–S8). Plio-Pleistocene bispectra were calculated to extract geometries, applying the following settings (after (27, 28)): resampling resolution = 2.5 kyr, window length = 1 Myr, step-size = 0.1 Myr, no blocks, degrees of freedom = 2, frequency resolution = 0.001 cycles/kyr (Fig. S5). The colors in the bispectral plots (Fig 2, Ext. Data Fig. 4) range from 1×10^{-5} to -1×10^{-5}. Rare values exceeding this range were set to match these maximum and minimum values to scale the color gradient to the part of the bispectrum where dominant interactions occur. In addition to couplings near eccentricity frequencies (see main text, $f_{\mathrm{ecc.}} = 2.5$ & ≈ 10.0 cycles/Myr), we observe some couplings between eccentricity and obliquity ($f_{\mathrm{obl.}} = 25.0$ cycles/Myr), which are indicated by; for example, the positive interactions at $B(25.0, 8.0)$ cycles/Myr in the mid-Oligocene and $B(25.0, 10.5)$ cycles/Myr in the OMT interval, where energy is transferred to $f_3 = 33.0$ and 35.5 cycles/Myr (~29 kyr/cycle), respectively. Precession ($f_{\mathrm{prec.}} \approx 50.0$ cycles/Myr) and obliquity are poorly expressed in the benthic $\delta^{18}O$ record of Site 1264 (15), which may explain their weaker definition in interactions (Fig. S4).

Non-sinusoidal cycle properties. Quantifying deviations from sinusoidality provides an objective way to describe cycle shapes (27, 28) or wave-forms (47). Walvis Ridge Site 1264 was tuned using one tie-point every ~125 kyr on average (15) and the cycle shapes of individual ~110-kyr cycles are therefore unaffected by the tuning approach. We calculate skewness, asymmetry and kurtosis of eccentricity, $CaCO_3$ est. and benthic $\delta^{18}O$ cycles across a 2-Myr sliding window (step-size 0.1 Myr) to track the evolving geometry of the cycles with the highest variance (i.e. the ~110-kyr cycles). This 2-Myr sliding window smooths the signal and may explain the gradual onset of asymmetry already at 24 Myr ago. We note that non-sinusoidal cycle properties are not frequency specific, as harmonics between multiple frequencies are needed to distort a sine-shaped cycle. They can, however, be attributed to frequency-bandwidths (48). Skewness and asymmetry are quantified using both standard and bispectral methods (47), to ascertain the reproducibility of the outcome. Kurtosis is quantified using the standard method only, as no trispectra were calculated. The 2σ upper and lower boundary error-ranges, calculated using a 2-Myr sliding window, were added to the long-term SiZer smooths of the (combined) geometry quantifications. Skewness is determined (49) as $Sk(x) = \frac{\langle(x-\bar{x})^3\rangle}{\langle(x-\bar{x})^2\rangle^{3/2}}$, where the overbar indicates the mean value and where < > is the time averaging operator. Asymmetry is determined (50) as $As(x) = \frac{\langle H^3(x-\bar{x})\rangle}{\langle(x-\bar{x})^2\rangle^{3/2}}$, where H is the Hilbert transform. Kurtosis is defined (51) as $k(x) = \frac{\langle(x-\bar{x})^4\rangle}{\langle(x-\bar{x})^2\rangle^2} - 3$. We extract skewness and asymmetry from the bispectrum following Eq. 3 of (47): $Sk(x) + iAs(x) = \left[12\sum_n \sum_l B(f_n\, f_l) + 6\sum_{p=1}^{\frac{N}{2}} B\left(f_p, f_p\right)\right] / E[x^2]^{3/2}$ where n and l range from 1 to the Nyquist frequency N, with $n > l$ and $n+l \leq N$. We note that not many studies since the pioneering work of (27, 28) on the late Pleistocene records, more recently reproduced using different statistical methods (32), have quantified non-sinusoidal glacial-interglacial cycle properties (such as sawtoothness). Most cyclostratigraphic studies have not commented on the non-sinusoidality of climate cycles or described these properties qualitatively.

SI Text:

Exploring potential cycle-shape distortion. A number of processes may act to distort the geometry of a glacial-interglacial signal recorded in marine sediments (52). To test for cycle-shape distortion in the stratigraphic domain caused by e.g. coring disturbances and/or (cyclic) changes in sedimentation rates, we computed the non-sinusoidal cycle properties of the X-ray fluorescence core scanning-derived $CaCO_3$ estimate tuning-signal curve (15) and compare these results to the non-sinusoidal cycle properties of the benthic

$\delta^{18}O$ record to evaluate whether the geometries in each of these records are independent from each other. Both the $CaCO_3$ est. and $\delta^{18}O$ records reveal strong cyclicity on eccentricity periodicities and therefore we also compare their geometries to those of the eccentricity tuning-target curve (8).

We note that the eccentricity solution, analyzed over a 2-Myr sliding window, has positive skewness, no asymmetry, and (overall) strong negative kurtosis (Fig. S6). Positive skewness for eccentricity over this window length is a counterintuitive result because individual ~110-kyr cycles are characterized by clear negative skewness. The $CaCO_3$ record shows an interval between ~24–18 Myr ago with positive skewness, which is preceded and followed by intervals between ~30–24 and 18–17 Myr ago with negative skewness (Fig. S7). Asymmetry of $CaCO_3$ est. does not show significant trends or offsets from zero. Kurtosis of $CaCO_3$ est. indicates mostly leptokurtic cycle shapes. The benthic $\delta^{18}O$ record from Site 1264, also analyzed over 2-Myr long windows, has very comparable skewness to eccentricity (Fig. S8). However, asymmetry and kurtosis show long-term trends independent from eccentricity. Leptokurtic cycles in $CaCO_3$ strongly contrast the platykurtic cycles found in eccentricity and (generally) in benthic $\delta^{18}O$. Overall, geometries of eccentricity (tuning target), $CaCO_3$ est. (tuning signal) and benthic $\delta^{18}O$ (climate proxy record) are largely independent from each other.

The inverse and (assumed) in-phase relationship between the $CaCO_3$ record and eccentricity (15) (where $CaCO_3$ maxima correspond to eccentricity minima) and the evolution of skewness, suggest (52) that the sediments at Site 1264 result from a productivity-dominated oceanographic setting, despite long-term trends in absolute values that may reflect a secondary influence of dissolution. Further evidence that the control of dissolution on $CaCO_3$ cycle shape during the Oligocene was smaller than that of productivity comes from the continuously high $CaCO_3$ values, and from the fact that Site 1264, at 2000–2200 meters paleo-water depth, was positioned well above the calcite compensation depth and lysocline throughout the entire Oligo-Miocene (14). We consider the dilution component by terrestrial input to be of a lesser influence on the preserved cycle shapes at Site 1264, as it is positioned far away from land. Physical, grain-size dependent, diffusion-like processes and bioturbation smooth the higher frequency paleoclimate signals in the natural archive (53). However, this probably did not affect cycle geometry in a preferential direction. Similarity in patterns between X-ray fluorescence core scanning records of overlapping intervals from both drill-holes (15) also rules out a significant effect of drilling disturbances on the deformation of specific intervals.

SI Figure Legends:

Fig. S1. Three-dimensional wavelet of δ^{18}O. Wavelet analysis of the Site 1264 benthic δ^{18}O record (21). Frequencies lower than 5 cycles/Myr (i.e. periodicities higher than 200 kyr/cycle) have been removed to emphasize the power on the ~10 cycles/Myr frequency (~110-kyr periodicity).

Fig. S2. Phase evolution of $CaCO_3$ est. with respect to eccentricity. (A) Phase-evolution of the 405-kyr cycle in the Site 1264 $CaCO_3$ est. record to that of eccentricity.

(B) Phase-evolution of the ~110-kyr cycle to eccentricity. (C) Phase-evolutions of the ~125-kyr and ~95-kyr cycles to eccentricity. The ~110-kyr cycle of $CaCO_3$ est. (panel B) is continuously coherent and in-phase within the 95% confidence level (i.e. ± 5 kyr of in-phase) with eccentricity, consistent with tuning-assumptions used (15). All further phase calculations (panels A and C this Fig., Fig. S3) are derived from this phase-assumption. Error bars represent the 95% Blackman-Tukey cross-spectral analysis confidence intervals. Phase calculations are only shown when coherent. Vertical gray bars as in Fig. 1.

Fig. S3. Phase evolution of $\delta^{18}O$ with respect to eccentricity. (A) Phase-evolution of the 405-kyr cycle in the Site 1264 benthic $\delta^{18}O$ record to that of eccentricity. (B) Phase-evolution of the ~110-kyr cycle to eccentricity. (C) Phase-evolutions of the ~125-kyr and ~95-kyr cycles to eccentricity, which show independent evolutions. Error bars represent the 95% Blackman-Tukey cross-spectral analysis confidence intervals. Phase calculations are only shown when coherent. Vertical gray bars as in Fig. 1.

Fig. S4. Bispectra assessing phase coupling and energy transfers between frequencies in the $\delta^{18}O$ data. Bispectral results over three 2-Myr long intervals that correspond to (A) ~2.4-Myr Eccentricity Cycle 9 (21.10 – 19.10 Myr ago, (B) Cycle 10 (23.54–21.54 Myr ago) and (C) Cycle 12 (28.30–26.30 Myr ago, see Methods). Gray lines reflect the main astronomical frequencies of eccentricity, obliquity and precession. The two panels of Fig. 2 in the main document are reproduced here (B and C) and expanded to include the interactions with the precession frequencies.

Fig. S5. Proof of methods in quantifying non-sinusoidal cycle properties. (A) Original skewness and asymmetry calculations on Plio-Pleistocene benthic and planktic $\delta^{18}O$ records (27). (B) Reproducing the results of (27) on the Plio-Pleistocene LR04 benthic $\delta^{18}O$ stack (54). Comparable results have been obtained using a different method (32). Triangles show asymmetry and circles show skewness. Turquoise indicates the standard method and purple-pink represents the bispectral method. Time (Ma) equates to Age (Myr ago).

Fig. S6. Non-sinusoidal cycle properties of eccentricity. (A) Orbital eccentricity (8), and (B) its skewness, (C) asymmetry, and (D) kurtosis, calculated across a 2-Myr sliding window using standard (turquoise circles) and bispectral methods (purple-pink triangles). An unexplained, small offset in skewness (panel A) is observed between values calculated using the standard and bispectral methods. Vertical gray bars as in Fig. 1.

Fig. S7 Non-sinusoidal cycle properties of $CaCO_3$ estimate record. (A) $CaCO_3$ est. from Site 1264, and (B) its skewness, (C) asymmetry, and (D) kurtosis, calculated across a 2-Myr sliding window using standard (turquoise circles) and bispectral methods (purple-pink triangles). Seven prominent, decimeter-thick chalk-layers are removed from the Oligocene part of the record prior to the quantification of non-sinusoidal cycle properties as these layers distort the background cyclicity. Vertical gray bars as in Fig. 1.

Fig. S8. Sinusoidal and non-sinusoidal cycle properties of benthic δ^{18}O. (A) Atmospheric CO_2 proxy estimates for the Oligo-Miocene and their long-term smooths (turquoise line and area, see Methods) through the reconstructed values and their maximum and minimum error estimates (black error bars). Gray diamonds represent phytoplankton CO_2 estimates, yellow squares are based on stomata and purple-red triangles represent CO_2 estimates based on paleosols (6, 7). Multiplication factors on the right refer to pre-industrial (p.-i.) CO_2 concentrations of 278 ppm. CE stands for Common Era. (B) Benthic foraminiferal δ^{18}O record from Site 1264, Walvis Ridge. (C) Earth's orbital eccentricity (8) and its ~2.4-Myr component (+0.02, brown bold italic cycle numbers). (D–F) Sinusoidal cycle properties. (D) Wavelet analysis of the Site 1264 benthic δ^{18}O record. Frequencies lower than 5 cycles/Myr (i.e. periodicities higher than 200 kyr/cycle) have been removed to emphasize the power on the ~10 cycles/Myr frequency (~110-kyr periodicity). (E) Gaussian filters (lines) and amplitude modulations (areas) of the combined ~95 kyr and ~125 kyr periodicities (centered around ~110 kyr) of the eccentricity solution (gray) and detrended benthic δ^{18}O data (blue). (F) Blackman-Tukey phase calculations across a 2-Myr sliding window (step size 0.25 Myr). 95% significance estimates are indicated. (G–I) Non-sinusoidal cycle properties. (F) Skewness, (H) asymmetry, and (I) kurtosis, calculated using standard (turquoise circles) and bispectral methods (purple-pink triangles). Corresponding cycle shapes are indicated on the right. ig = interglacial, g = glacial. Background areas indicate the 2σ upper and lower ranges of these non-sinusoidal cycle properties. (J-M) Four recurrent intervals during the Oligo-Miocene characterized by high-amplitude ~110-kyr cyclicity in benthic δ^{18}O (dark blue lines), compared to eccentricity (gray areas) and its ~2.4-Myr component (light brown areas). (J) The early Oligocene, contemporaneous with 405-kyr Eccentricity Cycle 73. (K) The mid-Oligocene, contemporaneous with Cycle 68. (L) The Oligo-Miocene transition, contemporaneous with Cycle 57. (M) The early Miocene, contemporaneous with Cycle 49. White numbers correspond to 405-kyr eccentricity cycles. To the right of panels B-I the Antarctic ice sheet and eccentricity conditions are suggested, and corresponding cycle shapes are depicted. Arrow indicates the direction of time. ig = interglacial, g = glacial. Vertical gray bars as in Fig. 1.

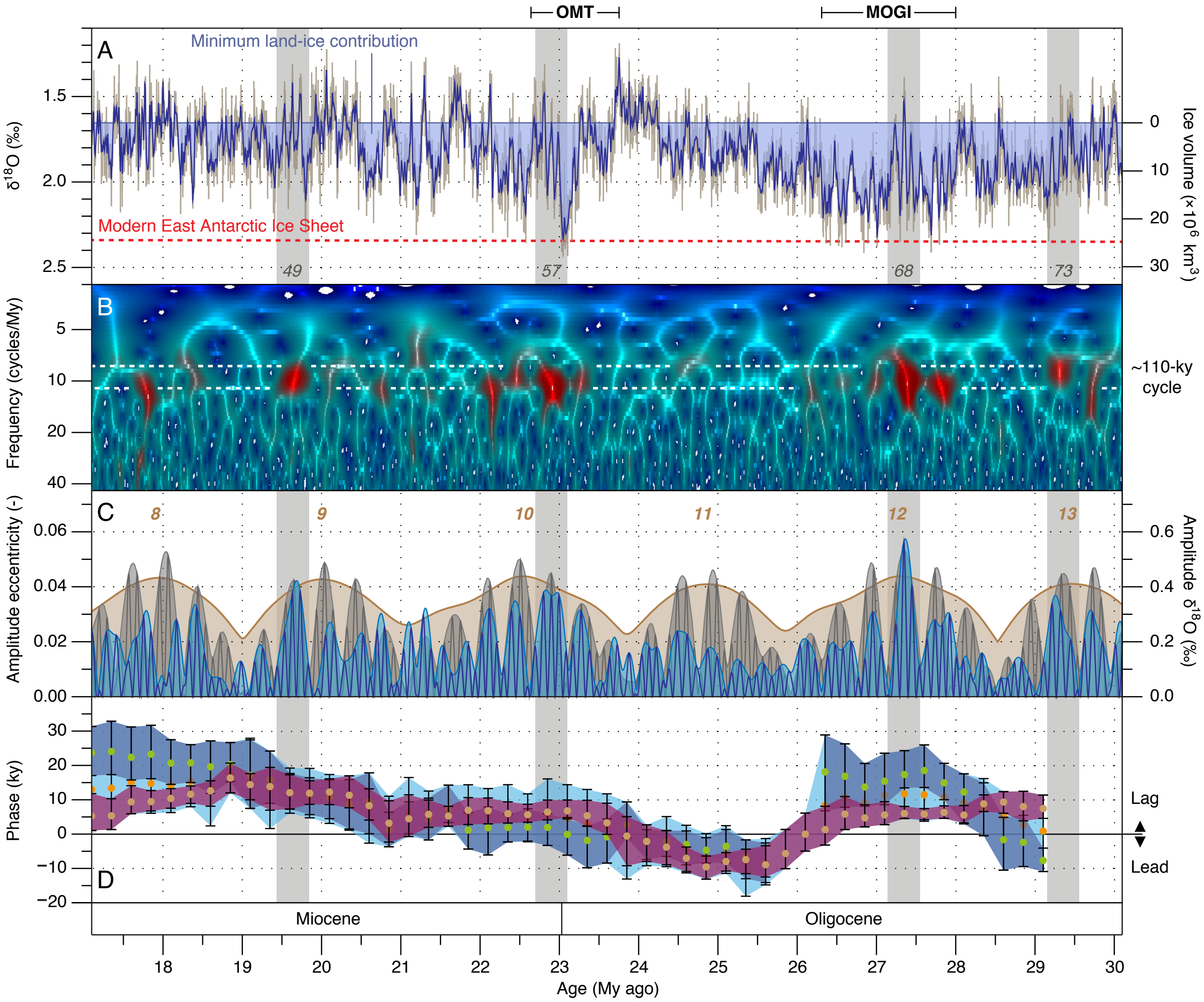
OMT
MOGI
A
Minimum land-ice contribution
δ18O (‰)
1.5
2.0
2.5
Modern East Antarctic Ice Sheet
49
57
68
73
Ice volume (×10^6 km^3)
0
10
20
30
B
Frequency (cycles/My)
5
10
20
40
~110-ky cycle
C
8
9
10
11
12
13
Amplitude eccentricity (-)
0.06
0.04
0.02
0.00
Amplitude δ18O (‰)
0.6
0.4
0.2
0.0
D
Phase (ky)
30
20
10
0
-10
-20
Lag
Lead
Miocene
Oligocene
18
19
20
21
22
23
24
25
26
27
28
29
30
Age (My ago)

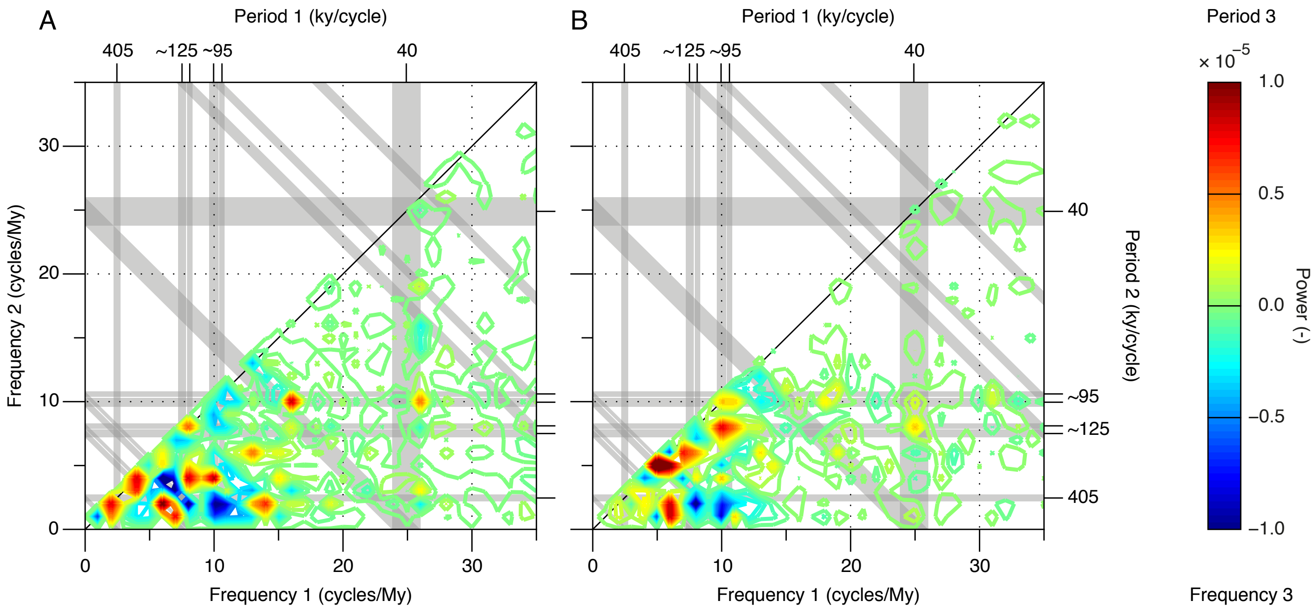
A
B
Period 1 (ky/cycle)
405
~125
~95
40
Frequency 2 (cycles/My)
0
10
20
30
Frequency 1 (cycles/My)
Period 2 (ky/cycle)
~95
~125
405
Period 3
× 10^{-5}
1.0
0.5
0.0
−0.5
−1.0
Power (-)
Frequency 3

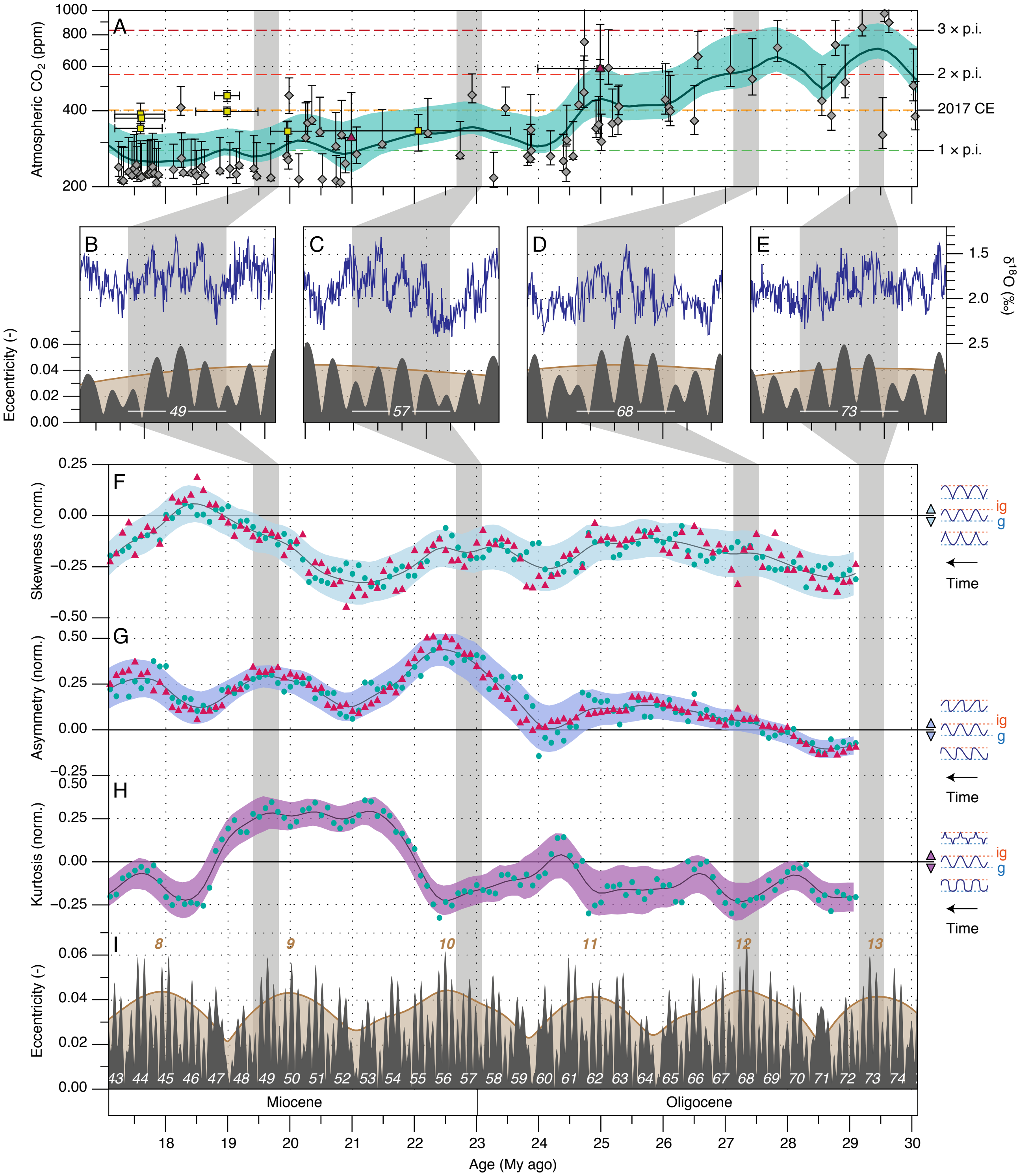
A
Atmospheric CO$_2$ (ppm)
1000
800
600
400
200
3 × p.i.
2 × p.i.
2017 CE
1 × p.i.
B
C
D
E
Eccentricity (-)
0.06
0.04
0.02
0.00
49
57
68
73
1.5
2.0
2.5
δ^{18}O (‰)
F
Skewness (norm.)
0.25
0.00
−0.25
−0.50
ig
g
Time
G
Asymmetry (norm.)
0.50
0.25
0.00
−0.25
ig
g
Time
H
Kurtosis (norm.)
0.50
0.25
0.00
−0.25
ig
g
Time
I
Eccentricity (-)
0.06
0.04
0.02
0.00
8
9
10
11
12
13
43 44 45 46 47 48 49 50 51 52 53 54 55 56 57 58 59 60 61 62 63 64 65 66 67 68 69 70 71 72 73 74
Miocene
Oligocene
18
19
20
21
22
23
24
25
26
27
28
29
30
Age (My ago)

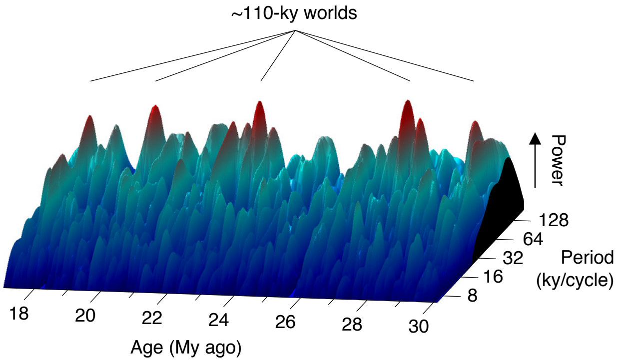
~110-ky worlds
Power
128
64
32
16
8
Period
(ky/cycle)
18
20
22
24
26
28
30
Age (My ago)

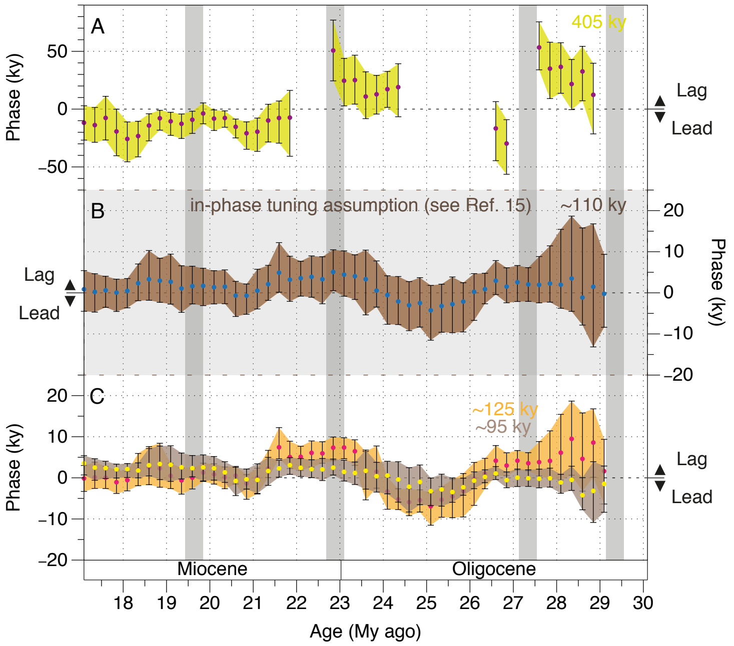
A
405 ky
Phase (ky)
50
0
−50
Lag
Lead
B
in-phase tuning assumption (see Ref. 15)
~110 ky
Lag
Lead
20
10
0
−10
−20
Phase (ky)
C
~125 ky
~95 ky
Phase (ky)
20
10
0
−10
−20
Lag
Lead
Miocene
Oligocene
18
19
20
21
22
23
24
25
26
27
28
29
30
Age (My ago)

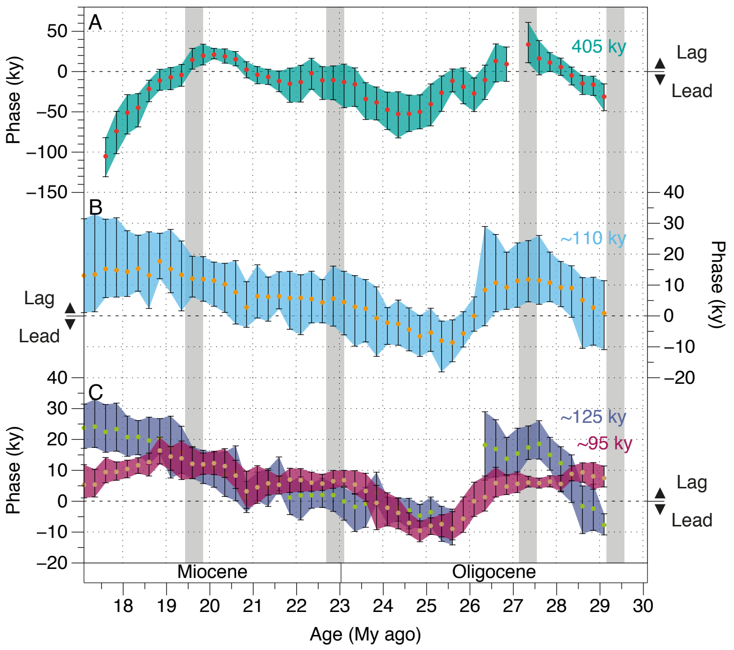
A
B
C
405 ky
~110 ky
~125 ky
~95 ky
Phase (ky)
Phase (ky)
Phase (ky)
50
0
−50
−100
−150
40
30
20
10
0
−10
−20
40
30
20
10
0
−10
−20
Lag
Lead
Lag
Lead
Lag
Lead
Miocene
Oligocene
18
19
20
21
22
23
24
25
26
27
28
29
30
Age (My ago)

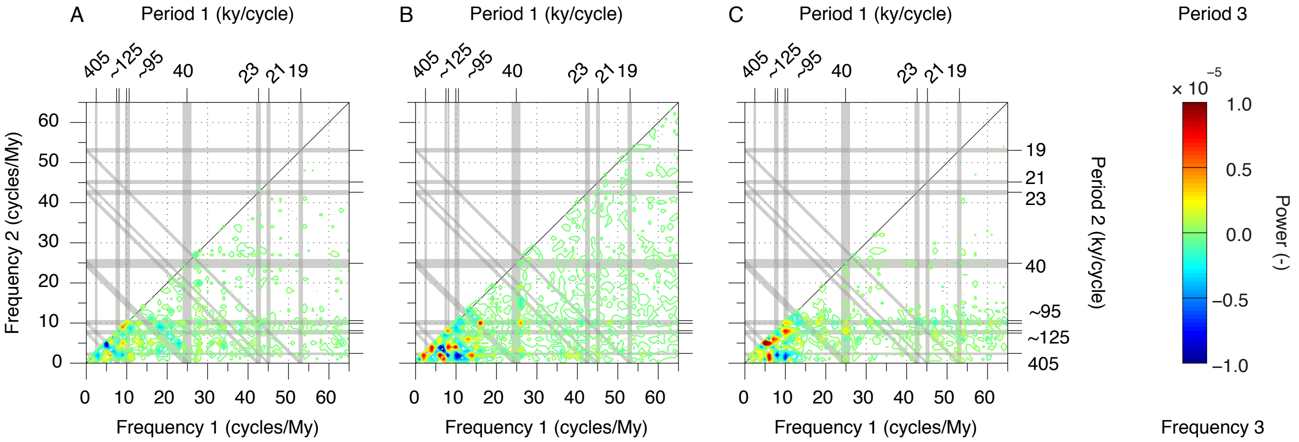
A
B
C
Period 1 (ky/cycle)
405
~125
~95
40
23
21
19
Frequency 1 (cycles/My)
Frequency 2 (cycles/My)
Period 2 (ky/cycle)
0
10
20
30
40
50
60
~95
~125
405
Period 3
× 10^−5
1.0
0.5
0.0
−0.5
−1.0
Power (-)
Frequency 3

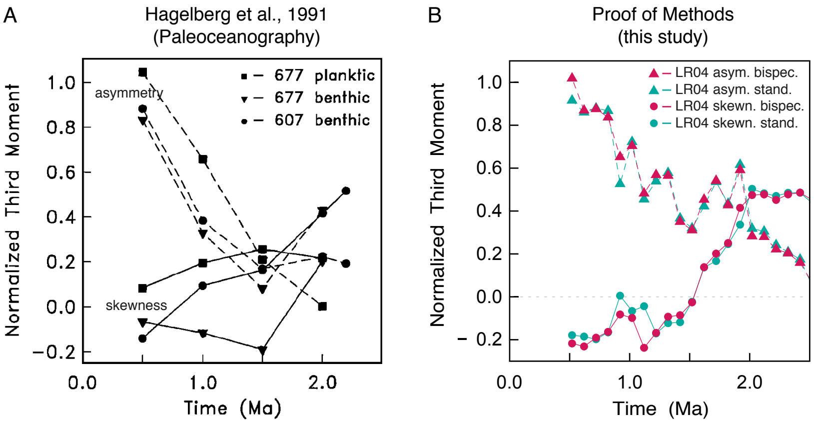
A
Hagelberg et al., 1991
(Paleoceanography)
Normalized Third Moment
1.0
0.8
0.6
0.4
0.2
0.0
−0.2
asymmetry
skewness
■ – 677 planktic
▼ – 677 benthic
● – 607 benthic
0.0
1.0
2.0
Time (Ma)
B
Proof of Methods
(this study)
Normalized Third Moment
1.0
0.8
0.6
0.4
0.2
0.0
- 0.2
▲ – LR04 asym. bispec.
▲ – LR04 asym. stand.
● – LR04 skewn. bispec.
● – LR04 skewn. stand.
0.0
1.0
2.0
Time (Ma)

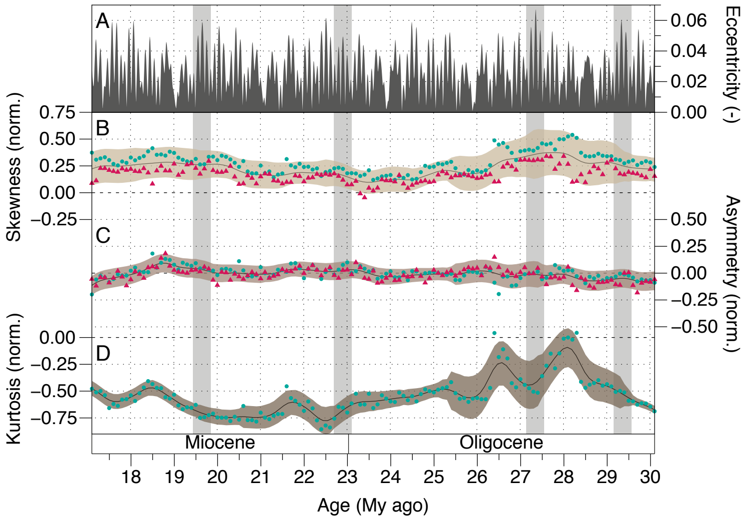
A
B
C
D
Eccentricity (-)
0.06
0.04
0.02
0.00
Skewness (norm.)
0.75
0.50
0.25
0.00
−0.25
Asymmetry (norm.)
0.50
0.25
0.00
−0.25
−0.50
Kurtosis (norm.)
0.00
−0.25
−0.50
−0.75
Miocene
Oligocene
18
19
20
21
22
23
24
25
26
27
28
29
30
Age (My ago)

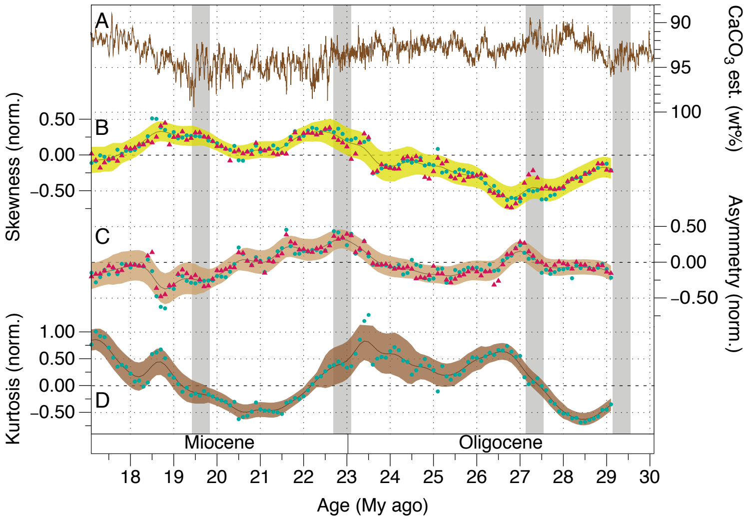
A
B
C
D
Skewness (norm.)
0.50
0.00
−0.50
Kurtosis (norm.)
1.00
0.50
0.00
−0.50
CaCO$_3$ est. (wt%)
90
95
100
Asymmetry (norm.)
0.50
0.00
−0.50
Miocene
Oligocene
18
19
20
21
22
23
24
25
26
27
28
29
30
Age (My ago)

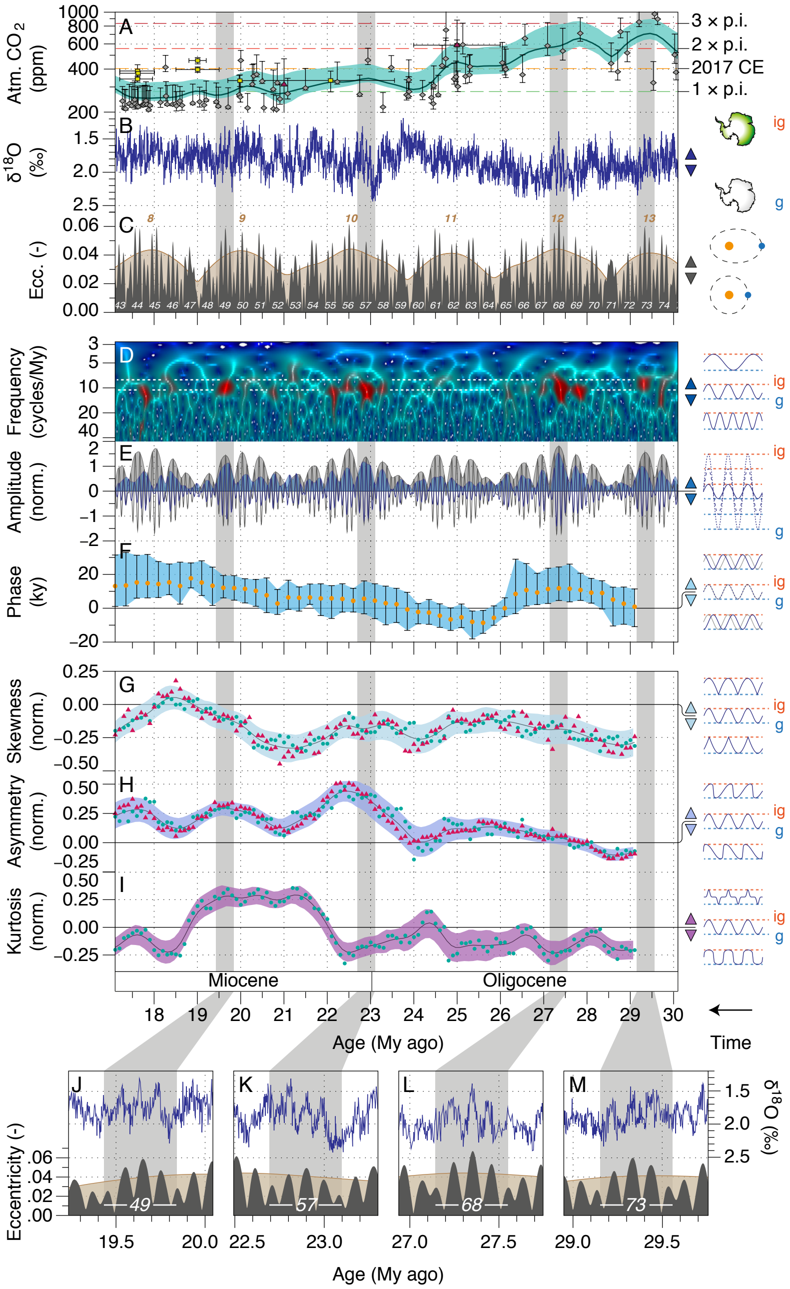
A
B
C
D
E
F
G
H
I
J
K
L
M
Atm. CO2 (ppm)
1000
800
600
400
200
3 × p.i.
2 × p.i.
2017 CE
1 × p.i.
δ18O (‰)
1.5
2.0
2.5
ig
g
Ecc. (-)
0.06
0.04
0.02
0.00
8
9
10
11
12
13
43 44 45 46 47 48 49 50 51 52 53 54 55 56 57 58 59 60 61 62 63 64 65 66 67 68 69 70 71 72 73 74
Frequency (cycles/My)
3
5
10
20
40
Amplitude (norm.)
2
1
0
−1
−2
Phase (ky)
20
0
−20
Skewness (norm.)
0.25
0.00
−0.25
−0.50
Asymmetry (norm.)
0.50
0.25
0.00
−0.25
Kurtosis (norm.)
0.50
0.25
0.00
−0.25
Miocene
Oligocene
18 19 20 21 22 23 24 25 26 27 28 29 30
Age (My ago)
Time
Eccentricity (-)
.06
.04
.02
.00
49
57
68
73
19.5
20.0
22.5
23.0
27.0
27.5
29.0
29.5
δ18O (‰)
1.5
2.0
2.5
Age (My ago)